Convective Heat Transfer in a Measurement Cell for Scanning Electrochemical Microscopy

Javor K. Novev and Richard G. Compton*

Department of Chemistry, Physical and Theoretical Chemistry Laboratory, Oxford University, South Parks Road, Oxford, OX1 3QZ, UK.

*Corresponding author. E-mail: Richard.Compton@chem.ox.ac.uk; Fax: +44 (0)1865 275 410; Tel: +44 (0)1865 275 957

Abstract: Electrochemical experiments, especially those performed with scanning electrochemical microscopy (SECM), are often carried out without taking special care to thermostat the solution; it is usually assumed that its temperature is homogeneous and equal to the ambient. The present study aims to test this assumption via numerical simulations of the heat transfer in a particular system – the typical measurement cell for SECM. It is assumed that the temperature of the solution is initially homogeneous but different from that of its surroundings; convective heat transfer in the solution and the surrounding air is taken into account within the framework of the Boussinesq approximation. The hereby presented theoretical treatment indicates that an initial temperature difference of the order of 1 K dissipates with a characteristic time scale of ~1000 s; the thermal equilibration is accompanied by convective flows with a maximum velocity of ~10^{-4} m·s^{-1}; furthermore, the temporal evolution of the temperature profile is influenced by the sign of the initial difference. These results suggest that, unless the temperature of the solution is rigorously controlled, convection may significantly compromise the interpretation of data from SECM and other electrochemical techniques, which is usually done on the basis of diffusion-only models.

I. Introduction

Scanning electrochemical microscopy (SECM) is a widely-used experimental technique that consists in measuring the faradaic current passing through a microelectrode when it is moved through an electroactive solution in relation to a substrate[1]. SECM has a wide range of applications, including topographic imaging of substrates, shape characterisation of microelectrodes, studies of living cells, measurements of the rates of surface reactions[1], etc. Measurements done with the scanning electrochemical microscope are generally interpreted under the assumption that throughout the experiment, the temperature of the solution is homogeneous and equal to the ambient[2] so that thermal convection does not

contribute to the mass transport. Few authors devote special attention to thermostating the solution in SECM measurements[2].

Despite that, some studies in which the temperature is controlled can be found in the literature; in most of them, the solution temperature is varied across a range of values. Notably, Zhang et al.[3] investigated an electron-transfer reaction at the interface between an organic liquid and a mixture of ice and a supporting electrolyte; this study involved a low-temperature electrochemical cell capable of maintaining temperatures down to -35 °C. Delville et al.[4] measured the temperature dependence of the rate of an electron-transfer reaction occurring across a monolayer at the interface of two immiscible electrolyte solutions. Wang et al.[5] did variable-temperature imaging of DNA hybridization via SECM; Hirano et al.[6] performed a low-temperature SECM study of living cells that used a custom-made heat bath. Kim et al.[7] constructed an isothermal chamber for SECM experiments in which the temperature varied by less than 0.3 K over the course of a whole day.

Other modifications of the SECM technique that involve thermal effects have been devised, e.g. Boika and Zhao[8] reported that using heated SECM tips, electrically insulating substrates can be distinguished based on differences in their thermal conductivities. Sode et al.[9] have determined the temperature distribution in the direction normal to the SECM tip through measurements of the open circuit potential in an SECM cell. Zhang et al.[10] have designed a microelectrode that also contains a thermocouple; if applied to SECM, such an electrode would give information on the local distribution of temperature in addition to the concentration profile that the standard measurements probe. Schäfer et al.[2] used a Peltier element to control the temperature of the sample and the solution in the SECM cell in an interval of over 100 K, taking special care to ensure that the temperature distribution was spatially homogeneous. In spite of that, the images they obtained at higher temperature were of lower resolution, which they ascribed to convection. In a follow-up study[11], the same research group took advantage of the fact the heating pulses that the Peltier element applies to the substrate cause it to expand. They improved the spatial resolution of the technique by synchronising the current acquisition with the oscillations of the substrate temperature.

In this study, we focus on the process of heat transfer in an SECM cell in contact with the ambient air, rather than the electrochemical reaction itself. Our aim will be to determine the timescale for reaching thermal equilibrium in a typical SECM measurement cell. We will suppose that initially there is small a temperature difference between the solution and its surroundings. In experimental studies with no temperature control it is implicitly assumed that even if such differences exist at the start of an experiment, they dissipate quickly and the temperature rapidly becomes homogeneous throughout the solution. If this assumption is violated, the resulting buoyancy flows will contribute to the measured electrical current, which is typically regarded as purely diffusive; they may also

result in a loss of imaging quality, as suggested by Schäfer et al.[2]. To our knowledge, no theoretical treatment of this particular problem has so far been published in the literature, despite its broad implications for the interpretation of SECM data in particular and for electrochemistry in general.

II.   Theoretical Model

1. Model

1.A.   *Heat Transfer*

In this section, we will present an approximate model of the heat transfer in a standard SECM measurement cell (CH Instruments, Inc., Austin, TX, USA, http://www.chinstruments.com), pictured in Figure 1A.

As we are most interested in simulating the behaviour of the studied system semi-qualitatively, rather than modelling all its details, we use a simplified model of the cell geometry that is expected to yield a realistic result. Ignoring the aperture at the bottom that exposes the studied substrate (see Figure 1A) and irregularities such as the semi-circular indentation in the wall that typically holds the reference electrode (not shown), we regard the cell as a cylinder of height h_{cell}, inner radius r_{cell} and outer radius $r_{cell} + d_{wall}$, filled with solution to a height of h_{cell}. While the actual cell is not filled to its full capacity, the volume of solution in our model corresponds to that in a typical measurement, see Section II.2 for more details. The cell is situated on top of a thermally insulating surface and is surrounded by a large body of air that acts as a heat bath. The measurement cell we model is made out of polytetrafluoroethylene; we approximate the material properties of the solution within it with those of pure water.

The temperature of the solution (T^L) is initially homogeneous, but different by ΔT from that of the cell (T^C) and the surrounding air (T^G), which at that moment are equal to T_∞. Over time, heat exchange causes T^L and T^G and therefore the densities of both fluids to become spatially inhomogeneous, thereby inducing convective flows.
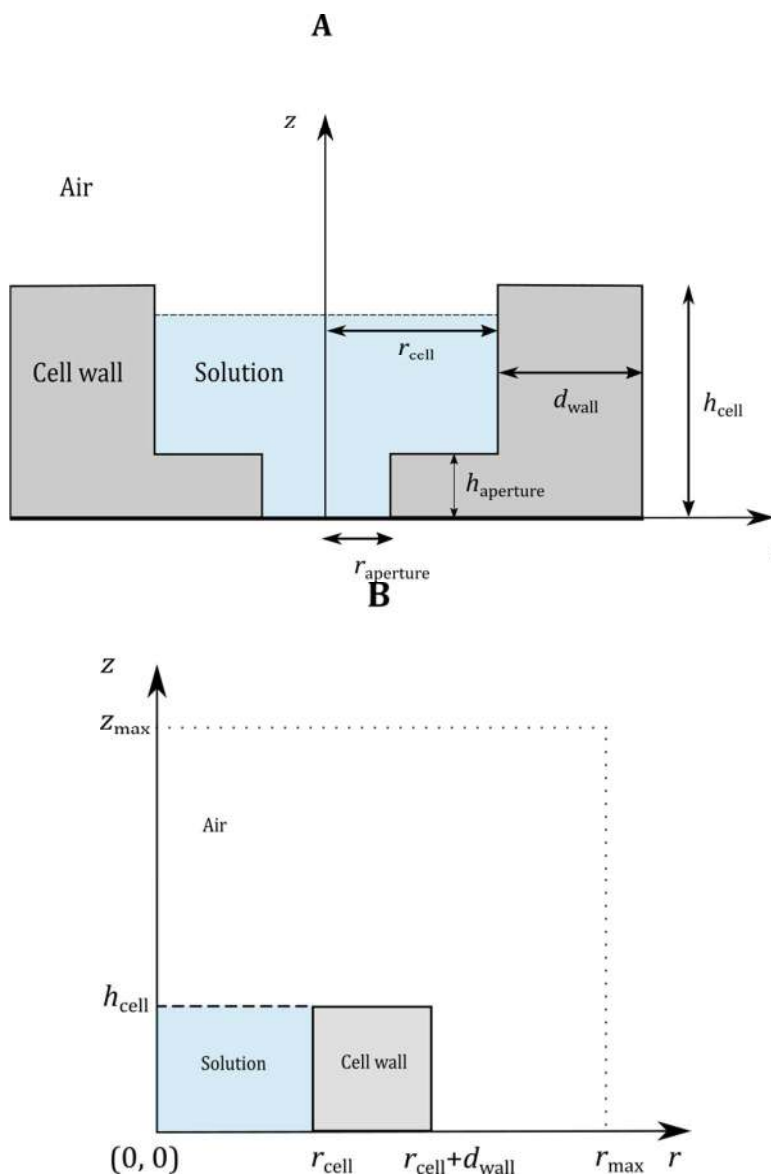
A

B

Figure 1. Schematic drawings of the geometry of an experimental cell (**A**) and the approximate geometry we adopt for the model (**B**).

The heat transfer in each of the three phases is governed by the convective heat equation,

$$\frac{\partial T^{\mathrm{i}}}{\partial t} + \boldsymbol{v}^{\mathrm{i}} \cdot \nabla T^{\mathrm{i}} = \chi^{\mathrm{i}} \nabla^2 T^{\mathrm{i}}, \tag{1}$$

where 'i' = L (liquid), G (gas) or C (cell), depending on the region in question, t denotes time, $\boldsymbol{v}^{\mathrm{i}}$ is the fluid velocity and χ^{i} is the respective thermal diffusivity [$m^2 \cdot s^{-1}$]. In the solid part of the cell, $\boldsymbol{v}^{\mathrm{C}} = \boldsymbol{0}$, and the heat transfer is purely conductive. We assume that the problem is axisymmetric; in that case, it is convenient to employ cylindrical coordinates (r,

ϕ, z); it follows from the symmetry of the problem that all quantities are independent of the polar angle ϕ and there is no fluid motion in its direction, $v_\phi = 0$.

The coordinate system is chosen so that its origin is at the centre of the cell bottom, and the vector of gravitational acceleration ($\boldsymbol{g}$) is aligned contrary to the positive z-direction.

For the temperature of the gaseous phase, the initial condition is

$$T^G(t = 0) = T_\infty. \tag{2}$$

In our model, the gas phase is treated as an infinite heat bath. For the purpose of solving the problem numerically, however, we restrict our treatment of the air to a cylinder of radius r_{max} and height z_{max} that extends far beyond the measuring cell, with $r_{max} \gg r_{cell} + d_{wall}$ and $z_{max} \gg h_{cell}$. At the boundaries of the simulated region, the temperature is presumed to be unaffected, which corresponds to the boundary conditions

$$T^G\big|_{z=z_{max}} = T^G\big|_{r=r_{max}} = T_\infty. \tag{3}$$

In addition, both the temperature and the heat flux must be continuous at the boundaries between the different phases[13], thus requiring that

$$(T^G - T^C)\big|_{r_{cell} < r < r_{cell} + d_{wall}, z = h_{cell}} = 0; \tag{4}$$

$$\left(\kappa^G \frac{\partial T^G}{\partial r} - \kappa^C \frac{\partial T^C}{\partial r}\right)\bigg|_{r_{cell} < r < r_{cell} + d_{wall}, z = h_{cell}} = 0; \tag{5}$$

$$(T^G - T^C)\big|_{r = r_{cell} + d_{wall}, 0 < z < h_{cell}} = 0; \tag{6}$$

$$\left(\kappa^G \frac{\partial T^G}{\partial z} - \kappa^C \frac{\partial T^C}{\partial z}\right)\bigg|_{r = r_{cell} + d_{wall}, 0 < z < h_{cell}} = 0, \tag{7}$$

$$(T^G - T^L)\big|_{0 < r < r_{cell}, z = h_{cell}} = 0; \tag{8}$$

where κ^i is the heat conductivity of the respective material.

At the air-liquid interface, the *total* heat flux, i.e., the sum of the convective and conductive contributions must be continuous,

$$\left(\kappa^G \frac{\partial T^G}{\partial z} + v_z^G \rho_0^G \Delta E^G - \kappa^L \frac{\partial T^L}{\partial z} - v_z^L \rho_0^L \Delta E^L\right)\bigg|_{0 < r < r_{cell}, z = h_{cell}} = 0, \tag{9}$$

where ΔE^i is the change of internal energy per unit mass for each fluid, with ρ_0^i being the density of the respective fluid at $t = 0$. However, we also require that no mass transfer

occurs though the air-water interface, which means that the normal velocities vanish at $z = h_{cell}$ (consult Section II.1.B) and eq. (9) simplifies to

$$\left(\kappa^G \frac{\partial T^G}{\partial z} - \kappa^L \frac{\partial T^L}{\partial z} \right) \Bigg|_{0 < r < r_{cell}, z = h_{cell}} = 0. \tag{10}$$

The air is assumed to be in contact with a perfectly thermally insulating solid surface at $z = 0$,

$$\partial_z T^G \Big|_{r_{cell} + d_{wall} < r < r_{max}, z = 0} = 0. \tag{11}$$

Due to the symmetry of the system, the temperature of the gas at the cell axis also obeys the condition

$$\partial_r T^G \Big|_{r = 0, h_{cell} < z < z_{max}} = 0. \tag{12}$$

We now turn our attention to the heat transfer in the liquid phase. At the start of the studied time period, the temperature of the liquid differs by ΔT from the ambient,

$$T^L(t = 0) = T_\infty - \Delta T, \tag{13}$$

where ΔT can be either positive or negative. Continuity of the temperature and the heat flux at the gas-liquid interface is ensured by eqs. (8)-(9); at the solid-liquid interface, we have to impose analogous boundary conditions,

$$(T^C - T^L) \Big|_{r = r_{cell}, 0 < z < h_{cell}} = 0; \tag{14}$$

$$\left(\kappa^C \frac{\partial T^C}{\partial r} - \kappa^L \frac{\partial T^L}{\partial r} \right) \Bigg|_{r = r_{cell}, 0 < z < h_{cell}} = 0. \tag{15}$$

The cell bottom situated at $z = 0$ is presumed to be a perfect thermal insulator, which means that

$$\partial_z T^L \Big|_{0 < r < r_{cell}, z = 0} = 0. \tag{16}$$

A symmetry condition analogous to eq. (12) applies to the temperature of the liquid,

$$\partial_r T^L \Big|_{r = 0, 0 < z < h_{cell}} = 0. \tag{17}$$

For the solid cell, the initial condition is identical to that for the gas,

$$T^C(t = 0) = T_\infty. \tag{18}$$

Continuity of the temperature and the heat flux at the solid walls is guaranteed by eqs. (4)-(7) and (14)-(15). The cell bottom is assumed to be a perfect thermal insulator,

$$\partial_z T^C \Big|_{r_{cell} < r < r_{cell} + d_{wall}, z = 0} = 0. \tag{19}$$

Note that in the treatment above, we have neglected the enthalpy change intrinsic to the electrochemical reaction itself; we have shown in a previous study that this is justified to a high level of approximation[14]. Furthermore, as the typical SECM electrode has a diameter of ~20 μm including its insulating sheath, whereas the diameter of the measurement cell is ~ 16 mm, the total heat flux through the tip is guaranteed to be negligible in comparison with the flux through the walls of the cell and through the liquid-gas interface.

1.B. *Momentum Transfer*

In this section, we will describe our approach to solving the hydrodynamic part of the problem under consideration.

As we stated in the Introduction, the heat transfer brings about temperature gradients in the liquid phases, which in turn cause density gradients and buoyancy forces to arise, a phenomenon known as free convection[13]. For that reason, the temperature profiles T^L, T^G and T^C must be determined by solving eqs. (1) in conjunction with the Navier-Stokes equations for the two fluid phases,

$$\rho_0^i \left(\frac{\partial \boldsymbol{v}^i}{\partial t} + \boldsymbol{v}^i \cdot \nabla \boldsymbol{v}^i \right) = -\nabla p^i + \eta^i \nabla^2 \boldsymbol{v}^i + \boldsymbol{F}^i, \tag{20}$$

where, as above, 'i' = L and G for the liquid and the gas, p^i is the hydrodynamic pressure in each phase, η^i is its viscosity, and $\boldsymbol{F}^i$ is the gravitational force that acts upon it. The force term is approximately given by the relation

$$\boldsymbol{F}^i = \rho_0^i \boldsymbol{g} \left[1 - \alpha^i \left(T^i - T^i(t = 0) \right) \right], \tag{21}$$

where α denotes the isobaric thermal expansion coefficient of the fluid, $\alpha = -1/\rho \, (\partial \rho / \partial T)_p$. For the solution we use the value for water at the initial temperature, $\alpha^L|_{T^L = (T_\infty - \Delta T)}$, while for the air, we use the ideal gas approximation, $\alpha^G \approx 1/T_\infty$.

The Navier-Stokes equations are paired with a continuity equation for each of the fluids,

$$\nabla \cdot \boldsymbol{v}^i = 0. \tag{22}$$

Eqs. (20)-(22) implicitly state that in our model, we only consider the variations in density with temperature insofar as buoyancy forces are concerned. We neglect the dependence of all other fluid properties on temperature, which is justified as long as $\left(T^i - T^i(t = 0) \right)/ T^i(t = 0)$ is sufficiently small, consult Gray and Giorgini[15]. Furthermore, eq. (22) also states that the gas phase is incompressible, which is evidently not true, but is sufficiently accurate for flows with a low Mach number like the ones we consider[16]. The system of equations

comprising eqs. (1) and (20)-(22) is known as the Boussinesq approximation for free convection[13,16].

Initially, neither of the fluid phases is in motion,

$$\boldsymbol{v}^{\mathrm{i}}(t=0) = \boldsymbol{0}. \tag{23}$$

The velocity of the air vanishes infinitely far away from the source of the disturbance (the measurement cell); in our numerical treatment of the problem, this condition is substituted with

$$\boldsymbol{v}^{\mathrm{G}}\big|_{r=r_{\max}} = \boldsymbol{v}^{\mathrm{G}}\big|_{z=z_{\max}} = \boldsymbol{0}. \tag{24}$$

To ensure that the model is equivalent to a measurement cell in contact with an infinite air bath, we choose the dimensions of the simulated region $r_{\max}$ and $z_{\max}$ as large as is computationally realistic such that $r_{\max} = 10 \cdot r_{\mathrm{cell}}$ and $z_{\max} = 40 \cdot z_{\mathrm{cell}}$, noting that these distances are of the order of the characteristic length of heat transfer, which for our simulations is $L \sim \sqrt{t\chi^{\mathrm{G}}} = \sqrt{3600 \cdot 2\mathrm{x}10^{-5}} \sim 0.2$ m.

No-slip boundary conditions equivalent to (24) are also required at the solid-air boundaries[13], namely at the walls of the cell and the insulating surface on top of which the cell is situated,

$$\boldsymbol{v}^{\mathrm{G}}\big|_{r_{\mathrm{cell}}<r<r_{\mathrm{cell}}+d_{\mathrm{wall}},z=h_{\mathrm{cell}}} = \boldsymbol{v}^{\mathrm{G}}\big|_{r=r_{\mathrm{cell}}+d_{\mathrm{wall}},0<z<h_{\mathrm{cell}}} = \boldsymbol{v}^{\mathrm{G}}\big|_{r_{\mathrm{cell}}+d_{\mathrm{wall}}<r<r_{\max},z=0} = \boldsymbol{0}. \tag{25}$$

Analogously, the velocity must vanish at the solid-liquid boundaries,

$$\boldsymbol{v}^{\mathrm{L}}\big|_{0<r<r_{\mathrm{cell}},z=0} = \boldsymbol{v}^{\mathrm{L}}\big|_{r=r_{\mathrm{cell}},0<z<h_{\mathrm{cell}}} = \boldsymbol{0}. \tag{26}$$

The fluid velocities are also subject to symmetry boundary conditions at the cylinder axis,

$$v_r^{\mathrm{i}}\big|_{r=0} = 0; \tag{27}$$

$$\frac{\partial v_z^{\mathrm{i}}}{\partial r}\bigg|_{r=0} = \frac{\partial v_r^{\mathrm{i}}}{\partial z}\bigg|_{r=0} = 0. \tag{28}$$

Equations (27)-(28) are analogous to eqs. 1.3-1.4 in Demkowicz's paper on symmetry conditions in Cartesian coordinates[17].

In addition to the conditions given so far, (24)-(28), we must specify boundary conditions at the liquid-gas interface. At the boundary between the two viscous fluids, the tangential velocity is continuous[18],

$$v_r^{\mathrm{L}}\big|_{z=h_{\mathrm{cell}}} = v_r^{\mathrm{G}}\big|_{z=h_{\mathrm{cell}}}. \tag{29}$$

Neglecting the mass transport between the two phases, we equate the normal velocities on both sides of the interface to zero,

$$v_z^L\big|_{z=h_{\text{cell}}} = v_z^G\big|_{z=h_{\text{cell}}} = 0. \tag{30}$$

Eq. (30) can be viewed as a special case of eq. 2.79 in the paper by Oron et al.[19] for a stationary interface through which there is no normal mass flux.

The kinematic boundary conditions (29)-(30) are complemented by the force balance at the surface. In the tangential direction, this reads

$$\eta^W\left(\frac{\partial v_z^L}{\partial r} + \frac{\partial v_r^L}{\partial z}\right)\Bigg|_{z=h_{\text{cell}}} = \eta^G\left(\frac{\partial v_z^G}{\partial r} + \frac{\partial v_r^G}{\partial z}\right)\Bigg|_{z=h_{\text{cell}}}, \tag{31}$$

i.e., the tangential viscous stress must be continuous at the interface. Eq. (31) neglects the effect of the interfacial tension on the flow. In a system like the presently discussed one, where the surface temperature is a function of the radial coordinate r, there is a non-zero gradient of the surface tension σ, which results in a force tangential to the interface and thermocapillary motion[18], otherwise known as the thermal Marangoni effect. Even though it may become important for surfactant-free surfaces like the one under consideration, we will neglect it here in the interest of simplicity.

In general, the normal stress balance for our system has the form[20]

$$\left(-p^L + 2\eta^L\frac{\partial v_z^L}{\partial z} + p^G - 2\eta^G\frac{\partial v_z^G}{\partial z}\right)\Bigg|_{z=h_{\text{cell}}} = 2\sigma H, \tag{32}$$

where H is the mean curvature of the interface[21]. Disregarding the variations in the hydrodynamic pressure due to buoyancy effects and noting that viscous stresses in the gas are negligible in comparison with those in the liquid leaves

$$\eta^L\frac{\partial v_z^L}{\partial z}\Bigg|_{z=h_{\text{cell}}} \approx \sigma H. \tag{33}$$

A dimensionless criterion, known as the capillary number[13], quantifies the ratio between the capillary and the viscous stress,

$$Ca = \frac{\eta^L U}{\sigma}, \tag{34}$$

where U is the characteristic normal velocity at the surface. The viscous stress is comparable to the capillary stress only if $Ca \sim 1$, which for water corresponds to $U \sim \sigma/\eta^L \sim 72$ m/s. The velocities in our case are orders of magnitude lower than this value (see Section III), and therefore $\sigma H \approx 0$ at all times, i.e. the surface behaves as non-deformable and remains flat. In this approximation, the hydrodynamic problem is completely defined

by the kinematic boundary conditions and the boundary condition for the lateral stress. As in the Rybczynski-Hadamard problem for a liquid drop moving through an ambient fluid, stating the shape of the surface in advance means that we cannot impose a boundary condition on the normal stress[20].

It should be noted that flows of the type studied here exhibit considerable complexity and axisymmetric modes may be inherently unstable. Their stability is determined by the values of the parameters of the system, and is particularly sensitive to the driving force ΔT and the aspect ratio of the cylindrical enclosure, h_{cell}/r_{cell}. It has been demonstrated by Neumann[22] that in a similar system, no axisymmetric flows can be stable at certain values of the aspect ratio. Furthermore, as shown by Yamaguchi et al.[23] for another system resembling the presently discussed one, even if the flows are assumed to be axisymmetric, they may exhibit complex patterns with multiple cells in both the radial and the axial direction. As we are most interested in establishing the order of magnitude of the flow velocity due to convection, we will assume that the flows are axisymmetric and we will not deal with the question of their stability, which goes beyond the aims of our study.

2. Simulations

This section gives a detailed description of the simulations we have performed and lists the values of the parameters we have used to that end.

Simulations of the heat transfer in an SECM measurement cell were performed with the commercial software package COMSOL Multiphysics ® 5.2[24]. The equations governing the transfer of heat and momentum in the system were solved numerically via the finite element method. Quadratic shape functions were used for the fluid velocity components and linear – for the hydrodynamic pressure; quintic shape functions were employed for the temperature distribution.

Rather than modelling the exact geometry of the cell (Figure 1A), we treated it as a cylinder filled with solution to its full capacity; for its height we used the value h_{cell} = 7 mm, for the inner radius – r_{cell} = 8 mm and for the wall thickness – d_{wall} = 7 mm. The parameters were chosen so as to guarantee that the total amount of solution in the model corresponded to that in a typical SECM experiment. For a standard measurement cell (CH Instruments, Inc.) as the one pictured in Figure 1A, r_{cell} = 8 mm, h_{cell} = 11 mm, $r_{aperture}$ = 3 mm, $h_{aperture}$ = 3 mm, d_{wall} = 7 mm[12]. Treating the aperture and the wider part of the cell as perfectly cylindrical, we can calculate that the total cell volume is V_{tot} = 1.69 mL; a cell is typically filled to approximately $V_{experimental}$ = 0.8·V_{tot}[12]. Approximating the cell with a cylinder of radius r_{cell} = 8 mm, we calculate that we need to set the model cell height to h_{cell} ≈ 7 mm in order to keep the volume in the model equal to $V_{experimental}$.

For all simulations, the simulated region was of dimensions $r_{max} = 10 \cdot r_{cell} = 8 \times 10^{-2}$ m by $z_{max} = 40 \cdot h_{cell} = 0.28$ m; though this finite configuration cannot give the exact pattern of convection in the air, we expect it to yield a correct result for the timescale of the heat transfer in the system, which is what we seek to determine.

For the ambient temperature, we used the value $T_\infty = 298.15$ K. Simulations were performed with $\Delta T = -5$ and 5 K, corresponding to an initial temperature of the solution higher and lower than the ambient, respectively. The properties of the liquid phase were approximated with those of water at the respective initial temperature, $T^L(t = 0) = T_\infty - \Delta T$. At $T^L(t = 0) = 293.15$ K, we used the values $\rho_0^L = 998.21$ kg·m^{-3}, $\eta^L = 1.002$ mPa·s, $\kappa^L = 0.5984$ W·m^{-1}·K^{-1} and $\alpha^L = 2.06 \times 10^{-4}$ K^{-1}, while at $T^L(t = 0) = 303.15$ K, we calculated with $\rho_0^L = 995.65$ kg·m^{-3}, $\eta^L = 0.7977$ mPa·s, $\kappa^L = 0.6154$ W·m^{-1}·K^{-1} and $\alpha^L = 3.02 \times 10^{-4}$ K^{-1}; the thermal diffusivity was calculated as $\chi^L = \kappa^L/(\rho_0^L C_p^L)$ with C_p^L (293.15 K) $= 4.1818 \times 10^3$ J·kg^{-1}·K^{-1} and C_p^L (303.15 K) $= 4.1784 \times 10^3$ J·kg^{-1}·K^{-1} [25].

The density of the air was taken to be $\rho_0^G = 1.161$ kg·m^{-3}; the values $\eta^G = 18.6$ μPa·s, $\kappa^G = 2.62 \times 10^{-2}$ W·m^{-1}·K^{-1} and $C_p^G = 1.007 \times 10^3$ J·kg^{-1}·K^{-1} were used for its heat conductivity and heat capacity, respectively[25].

As a typical SECM measurement cell (CH Instruments, Inc.), the cell in our model is made of polytetrafluoroethylene, for which $\rho^C = 2200$ kg·m^{-3} [26], $\kappa^C = 0.259$ W·m^{-1}·K^{-1} [27] and $C_p^C = 898.1$ J·kg^{-1}·K^{-1} [28].

The duration of the simulated experiment was 3600 s in each case. Simulations that involved conductive heat transfer only in all phases were run for comparison; for that case, eq. (1) was solved with the initial and boundary conditions (2)-(19) and $\boldsymbol{v}^i$ set to **0**.

III.   Results and Discussion

The heat transfer across the whole solution is best illustrated by the volume-averaged dimensionless temperature change,

$$\Delta T_{av} = \left| \frac{\int_V \left(T^L - T^L(t=0)\right) dV}{\int_V \left(T^L(t=0) - T_\infty\right) dV} \right| = \frac{1}{\pi r_{cell}^2 h_{cell}} \frac{1}{\Delta T} \int_V \left(T^L - T^L(t=0)\right) dV, \tag{35}$$

where the integration is over the cylindrical cell volume. It is evident from this definition that ΔT_{av} goes from 0 at the start of the process ($t = 0$) to 1 at as the system approaches thermal equilibrium ($t \to \infty$). Eq. (35) is plotted as a function of time in Figure 2 for the various investigated cases. As ΔT_{av} varies by less than a percent between the conduction-only simulations depending on the sign of the initial temperature difference ΔT, only the

curve corresponding to ΔT = -5 K is shown in the figure. Figure 2 demonstrates that in the simulation with the full model, the timescale for reaching thermal equilibrium is of the order of 10^3 s. The heat transfer becomes significantly affected by convection after a time period of $\sim$ 100 s that is necessary for the flow patterns to be established. After that initial period, the average temperature difference ΔT_{av} differs by as much as 10 % between the convective simulations and the one with conduction only. Furthermore, it is evident from the plot that the magnitude of the convective contribution to ΔT_{av} depends on the sign of the initial temperature difference between solution and surroundings.
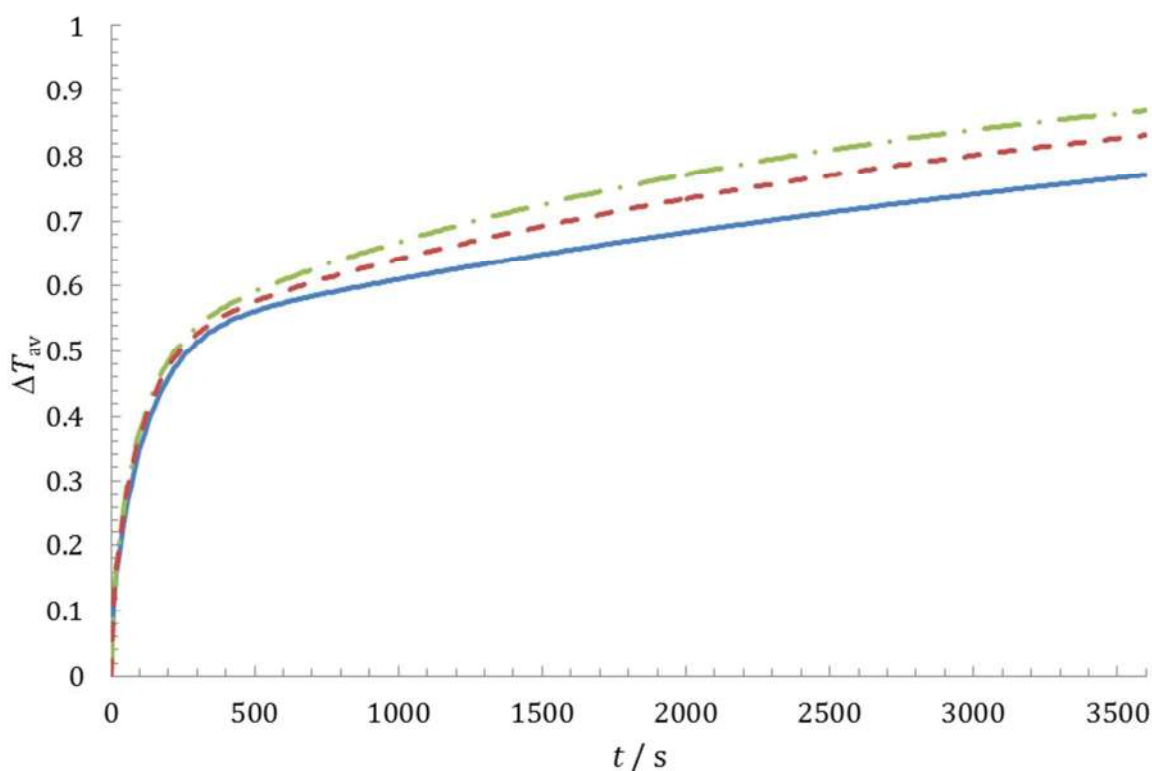

Figure 2. ΔT_{av} plotted against t for three investigated cases: purely conductive heat transfer (solid line) and heat transfer with convection in a solution that is colder (dashed line, ΔT = 5 K) or warmer (dashdot line, ΔT = -5 K) than its surroundings at t = 0. Note that convection enhances the heat transfer in both cases, but does so to a greater extent if $\Delta T <$ 0. The reason for that is the more intense flow that corresponds to this configuration, see the text.

This dependence is easily explainable in qualitative terms – if at t = 0, the solution is colder than the surrounding air ($\Delta T >$ 0), the liquid layers adjacent to the interface start to become warmer and become less dense, meaning that they experience a buoyancy force directed upwards (eq. (21)), but as they are already situated at the top of the cell, this does not cause intense mixing in the liquid; the opposite is true for the case with $\Delta T <$ 0. As the convective flows play an important role for the overall heat transfer, starting with a warmer solution ($\Delta T <$ 0) leads to faster equilibration, see Figure 2.

Figures 3-7 illustrate this point by showing the evolution of the temperature and the flow in the studied system. A dimensionless quantity,

$$\tilde{T} = \frac{1}{\Delta T}\left(T - T^{L}(t=0)\right),\tag{36}$$

is plotted in the figures rather than the temperature profiles themselves. $\tilde{T}$ is the local equivalent of ΔT_{av} (eq. (35)); at $t = 0$, it varies between 0 for the liquid and 1 for the solid cell and air; at thermal equilibrium, $\tilde{T}$ would be equal to 1 throughout the system. Figure 3 shows 'snapshots' of the spatial distribution of $\tilde{T}$ corresponding to purely conductive heat transfer at $\Delta T = -5$ K; just as ΔT_{av}, $\tilde{T}$ depends very weakly on the initial difference for the convection-free simulations; for that reason, the case with $\Delta T = 5$ K is not illustrated. Figures 4 and 5 contain plots of $\tilde{T}$ for simulations that involve convection with initial conditions corresponding to a solution that is respectively warmer and colder than the surroundings. It is clear from Figures 3-5 that the temperature profile in the gaseous phase is considerably distorted by the inclusion of convection in the model, but those in the liquid and the cell are not strongly affected. In qualitative terms, this can be explained by calculating the Péclet numbers that compare the importance of convective and conductive heat transport in the two phases. For the heat transport in the gas phase at $t \sim 100$ s,

$$Pe^{G} = \frac{z_{max}|v^{G}|}{\chi^{G}} \sim 100,\tag{37}$$

whereas for the liquid phase,

$$Pe^{L} = \frac{h_{cell}|v^{L}|}{\chi^{L}} \sim 10,\tag{38}$$

where we have used the orders of magnitude of the velocities from Figures 6-9. As Pe^{G} is an order of magnitude larger than Pe^{L}, convective heat transport is much more important for the gaseous phase than for the liquid phase.

Comparison between Figures 2-3 for the dimensionless temperature profile $\tilde{T}$ and Figures 6-7 for v^{G} shows that the shape of the temperature profile in the air is largely determined by the convective flow. These figures also demonstrate the differences in the intensity of the flow and the length scale to which the initial disturbance propagates depending on the sign of ΔT. For $\Delta T = -5$ K, i.e., for a solution warmer than its surroundings at $t = 0$, the maximum velocity $|v^{G}_{max}|$ is of the order of 4×10^{-2} m·s^{-1} and the flow encompasses the whole height of the cell ($\sim 10^{-1}$ m), while for $\Delta T = 5$ K $|v^{G}_{max}|$ only reaches about 6×10^{-3} m·s^{-1}, and the flow is restricted to the lower region of the cell ($\sim 10^{-2}$ m); the direction of the circulation inside the simulated region of the cell also changes with the sign of ΔT.

Figures 8 and 9, which contain 'snapshots' of v^L, demonstrate the effect the sign of the initial temperature change exerts on the flow patterns in the liquid phase. As in the gas phase, the direction of the flow in the simulated part of the cylinder and the magnitude of the maximum velocity are predicted to depend on the sign of ΔT, but the overall patterns are similar ($|v^L_{max}| \sim 3 \times 10^{-4}$ vs. 2×10^{-4} m·s^{-1}).

As the system approaches equilibrium, the temperature gradients in all phases diminish, and so do the convective flows, as illustrated by the plots at $t = 3600$ s in Figures 6-9.

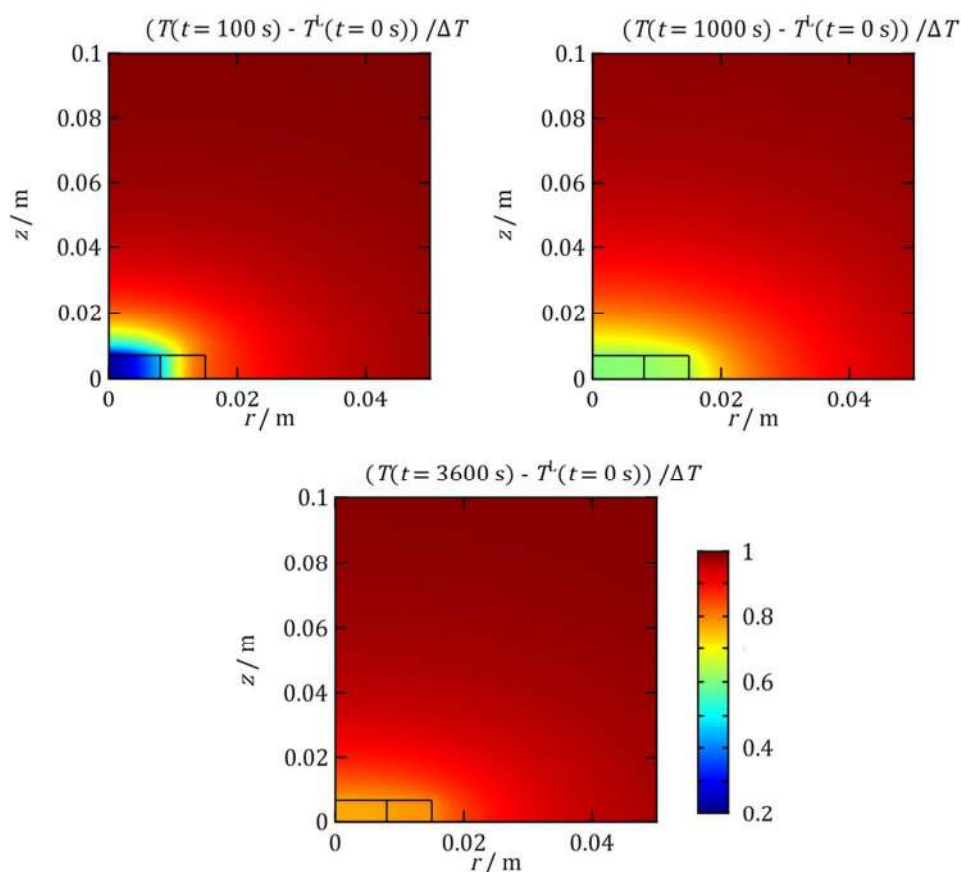Figure 3. 'Snapshots' of the dimensionless temperature distribution, $\tilde{T} = (T - T^L(t = 0))/\Delta T$ at $t = 100$ s, $t = 1000$ s and $t = 3600$ s as predicted by a simulation including only heat transfer by conduction.
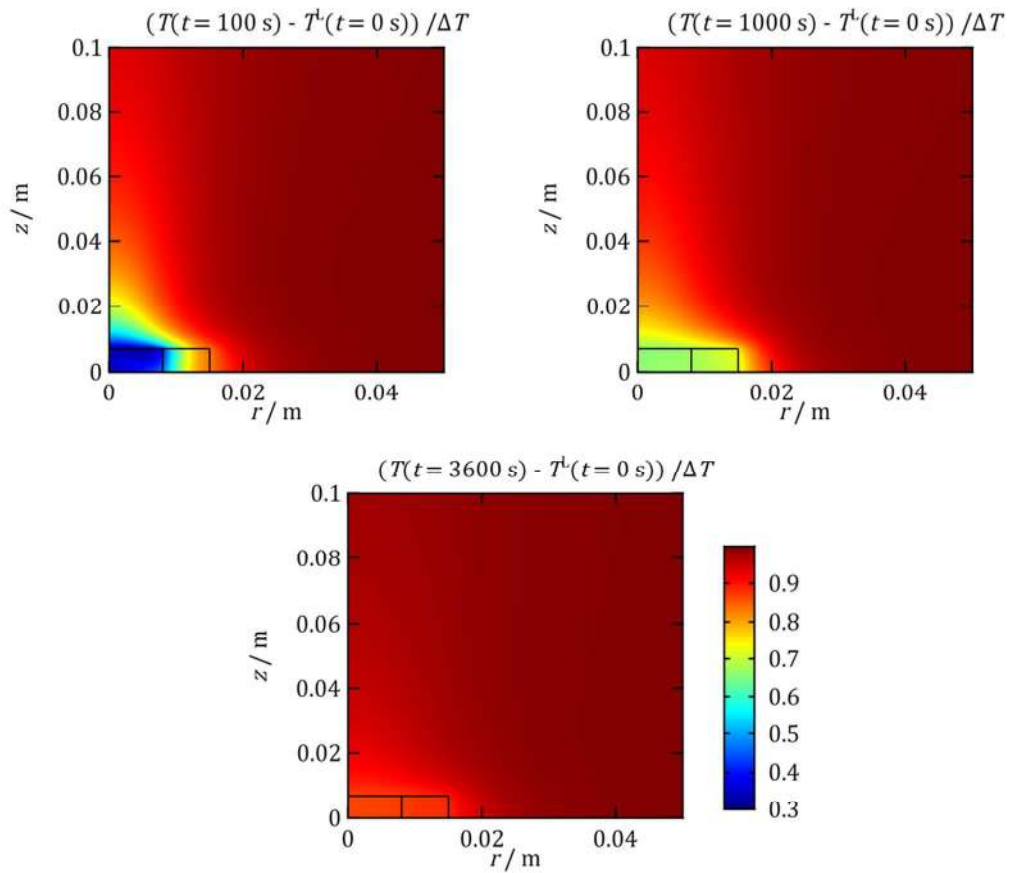
Figure 4. Dimensionless temperature distribution, $\widetilde{T} = (T - T^L(t = 0))/\Delta T$, plotted at $t = 100$ s, $t = 1000$ s and $t = 3600$ s for $\Delta T = -5$ K, i.e. for a solution that is initially warmer than its surroundings.
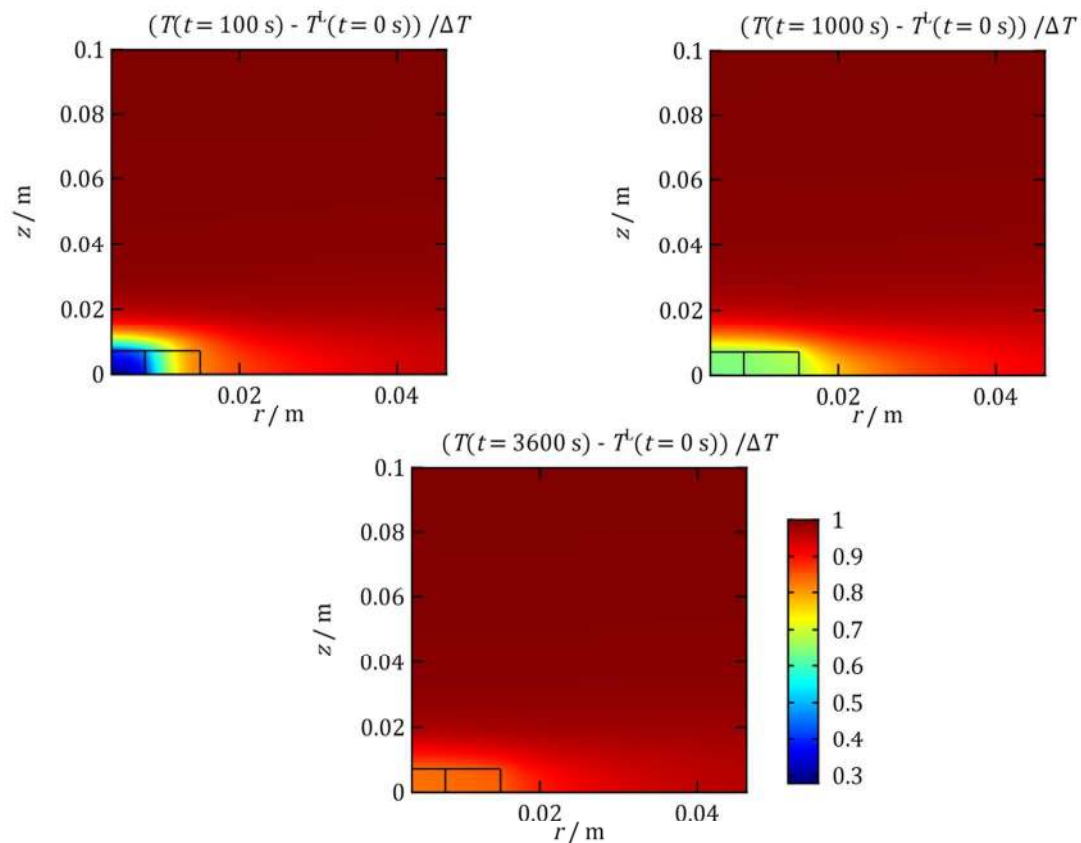
$(T(t = 100 \text{ s}) - T^L(t = 0 \text{ s}))/\Delta T$

$(T(t = 1000 \text{ s}) - T^L(t = 0 \text{ s}))/\Delta T$

$(T(t = 3600 \text{ s}) - T^L(t = 0 \text{ s}))/\Delta T$

Figure 5. Dimensionless temperature distribution, $\tilde{T} = (T - T^L(t = 0))/\Delta T$, plotted at $t = 100$ s, $t = 1000$ s and $t = 3600$ s for $\Delta T = 5$ K, i.e. for a solution that is initially colder than its surroundings.
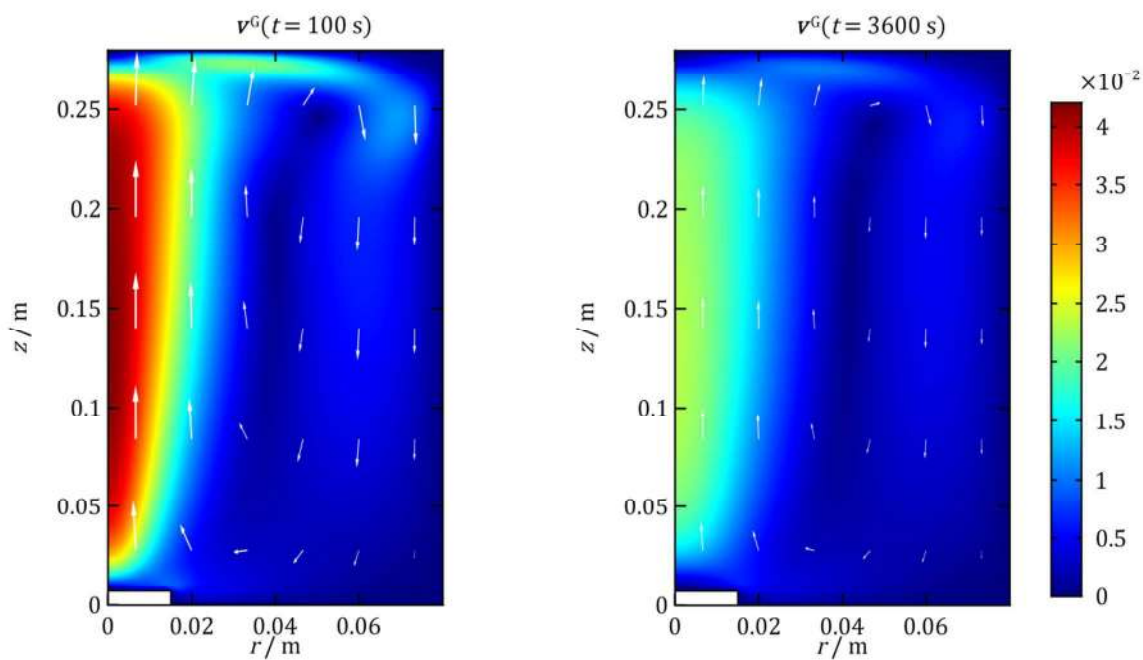

$v^G(t = 100 \text{ s})$

$v^G(t = 3600 \text{ s})$

Figure 6. Velocity field in the gas phase (v^G) plotted at t = 100 s and t = 3600 s for ΔT = -5 K, i.e. for a solution that is initially warmer than its surroundings. The length of the arrows is proportional to the natural logarithm of $|v^G|$.
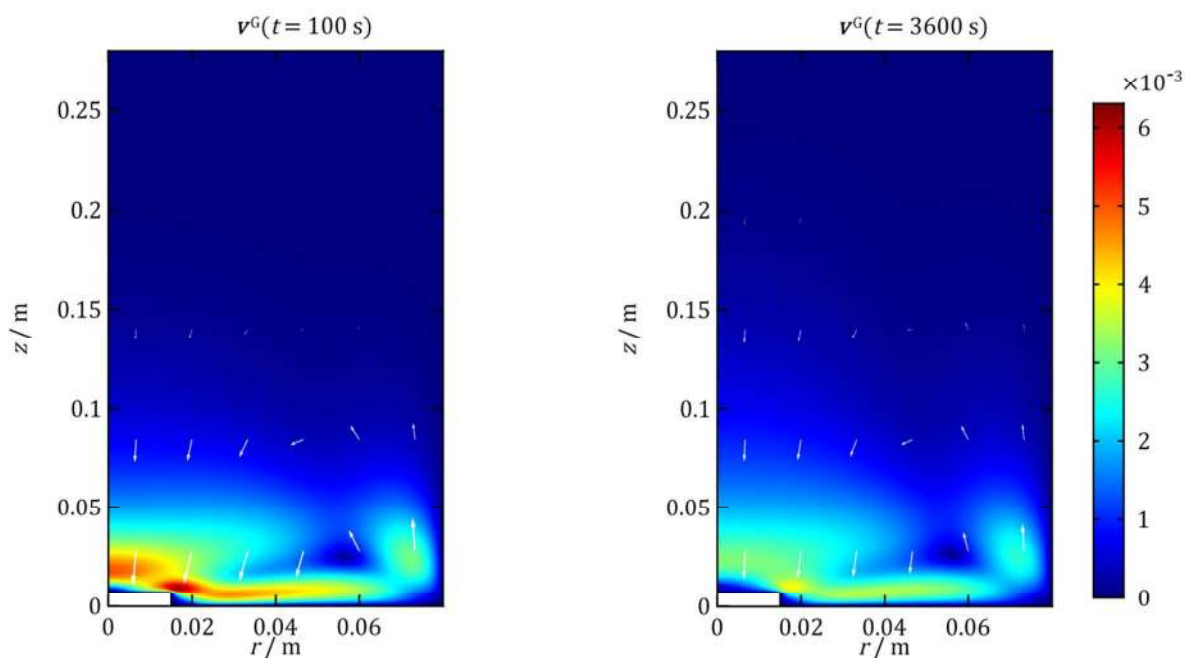

Figure 7. Velocity field in the gas phase (v^G) plotted at t = 100 s, and t = 3600 s for ΔT = 5 K, i.e. for a solution that is initially colder than its surroundings. The length of the arrows is proportional to the natural logarithm of $|v^G|$.
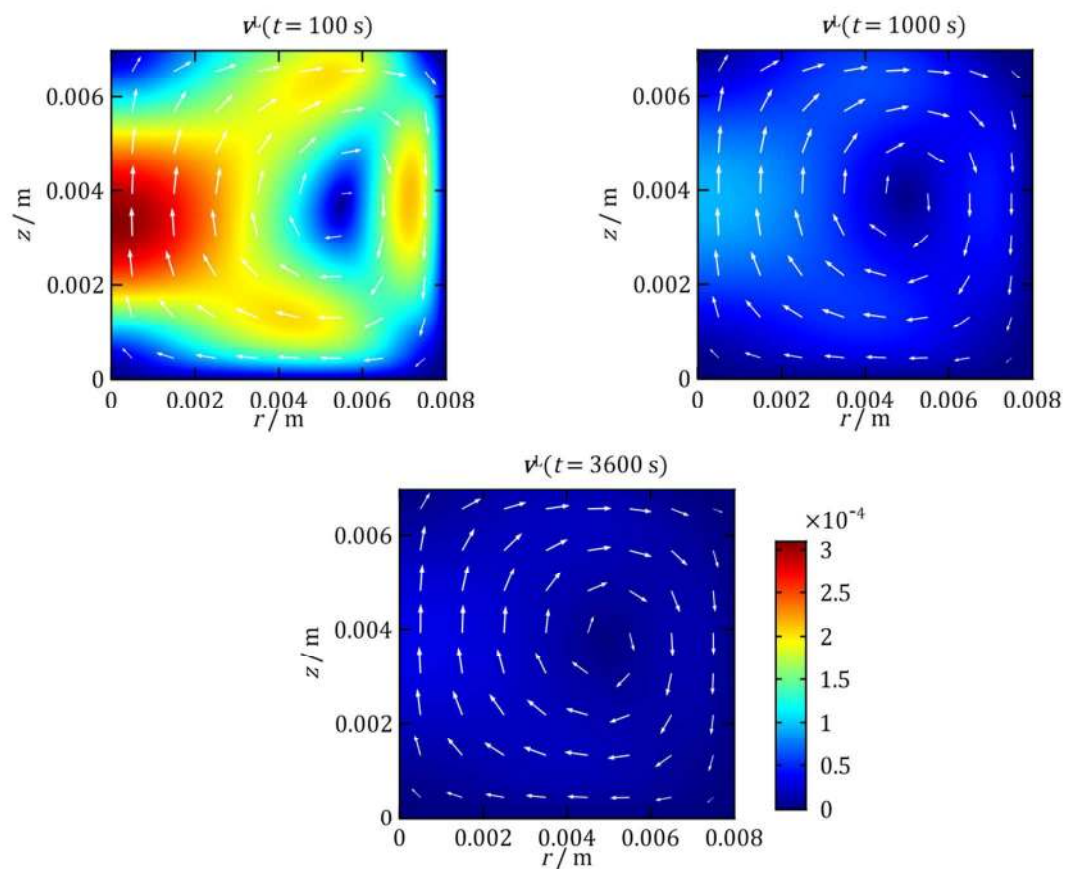
Figure 8. Velocity in the liquid phase (v^L) plotted at $t = 100$ s, $t = 1000$ s and t = 3600 s for ΔT = -5 K, i.e. for a solution that is initially warmer than its surroundings. The length of the arrows is proportional to the natural logarithm of $|v^L|$.
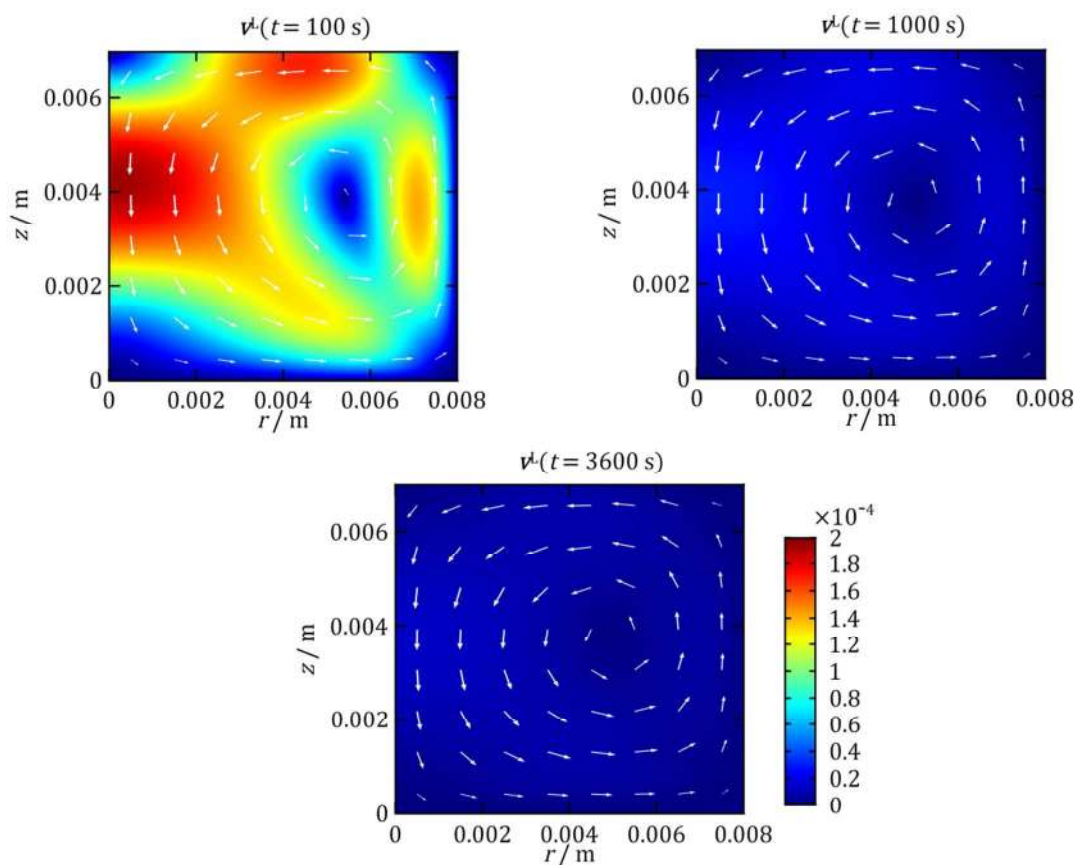
Figure 9. Velocity field in the liquid phase (v^L) plotted at $t = 100$ s, $t = 1000$ s and t = 3600 s for $\Delta T = 5$ K, i.e. for a solution that is initially colder than its surroundings. The length of the arrows is proportional to the natural logarithm of $|v^L|$.

IV.   Conclusions

We have investigated the heat transfer in a typical SECM measuring cell by performing numerical simulations based on an approximate model. We have demonstrated that, if there is an initial difference between the temperature of the solution and its surroundings, (ΔT, with $|\Delta T| \sim 1$ K), the characteristic time for reaching thermal equilibrium is of the order of one hour. Our treatment of the conjugate heat and momentum transfer in the system within the framework of the Boussinesq approximation indicates that a significant amount of heat is transported via convection, and that the intensity of the convective heat transfer depends on the sign of ΔT because the intensity of the convective flows in the cell and the surrounding air is determined by the initial temperature distribution.

Most SECM experiments do not include thermostating of the solution either by use of a special design for that purpose or by waiting for thermal equilibrium to set in[2], assuming instead that the temperature throughout the liquid phase is homogeneous and equal to the ambient. As we have shown, this assumption is incorrect and may lead to

substantial errors in the determination of temperature-sensitive qualities such as reaction rate constants, not least since the solution viscosity is strongly temperature-sensitive (see for example Kampmeyer's paper[29] on the viscosity of pure water) and therefore the same is true of the diffusion coefficients of electroactive species. Moreover, as temperature-generated buoyancy forces induce velocities as high as 10^{-4} m·s^{-1} in the solution (during the initial ~ 100 s), there will also be a convective contribution to the electrical currents measured at the SECM tip. Thus, imperfect thermostating can render the diffusion-only mass transport models typically used to interpret SECM data inapplicable; it can also lead to the 'smearing out' or even the loss of the images obtained via the technique. Our results also raise questions about the interpretation of data from other electrochemical experiments for which no special care for thermostating is taken.

Physical Chemistry Chemical Physics Accepted Manuscript

References

1. A.J. Bard, M.V. Mirkin (Eds.), *Scanning Electrochemical Microscopy*, 2nd Edition, CRC Press, Boca Raton, 2012.
2. D. Schäfer, A. Puschhof and W. Schuhmann, *Phys. Chem. Chem. Phys.*, 2013, **15**, 5215.
3. Z. Zhang, J. Ye, P. Sun, Y. Yuan, Y. Tong, J. Hu and Y. Shao, *Anal. Chem.*, 2002, **74**, 1530.
4. M.-H. Delville, M. Tsionsky and A.J. Bard, *Langmuir*, 1998, **14**, 2774.
5. J. Wang, F. Song and F. Zhou, *Langmuir*, 2002, **18**, 6653.
6. Y. Hirano, Y. Nishimiya, K. Kowata, F. Mizutani, S. Tsuda and Y. Komatsu, *Anal. Chem.*, 2008, **80**, 9349.
7. J. Kim, M. Shen, N. Nioradze and S. Ameiya, *Anal. Chem.*, 2012, **84**, 3489.
8. A. Boika and Z. Zhao, *Electrochem. Commun.*, 2016, **68**, 36.
9. A. Sode, M. Nebel, P. Pinyou, S. Schmaderer, J. Szeponik, N. Plumeré and W. Schumann, *Electroanalysis*, 2013, **25**, 2084.
10. H. Zhang, X. Xiao, T. Su, X. Gu, T. Jin, L. Du and J. Tang, *Electrochem. Commun.*, 2014, **47**, 71.
11. J. Clausmeyer, D. Schäfer, M. Nebel and W. Schuhmann, *ChemElectroChem*, 2015, **2**, 946.
12. A.J. Wain, National Physical Laboratory, Teddington, Middlesex, TW11 0LW, United Kingdom. Personal communication, 2016.
13. R. B. Bird, W.E. Stewart and E.N. Lightfoot, *Transport Phenomena*, 2nd Edition, Wiley, New York, NY, 2002.
14. J.K. Novev, S. Eloul and R.G. Compton, *J. Phys. Chem. C*, 2016, **120**, 13549.
15. D.D. Gray and A. Giorgini, *Int. J. Heat Mass Transfer*, 1976, **19**, 545.
16. P. K. Kundu and I. M. Cohen, *Fluid Mechanics*, 2nd Edition, Academic Press, San Diego, CA, 2002.
17. L.A Demkowicz, *Appl. Math. Lett.*, 1991, **4**, 27.
18. V.G. Levich, *Physicochemical Hydrodynamics*, Prentice-Hall, Inc., Englewood Cliffs, NJ, 1962.
19. A. Oron, S.H. Davis and S. George Bankoff, *Rev. Mod. Phys.*, 1997, **69**, 931.
20. G.K. Batchelor, *An Introduction to Fluid Dynamics*, Cambridge University Press, Cambridge, 2000.
21. P. Kralchevsky and K. Nagayama, *Particles at Fluid Interfaces and Membranes*, Elsevier, Amsterdam, 2001.
22. G. Neumann, *J. Fluid Mech.*, 1990, **214**, 559.
23. Y.Yamaguchi, C.J. Chang and R.A. Brown, *Phil. Trans. R. Soc. Lond. A*, 1984, **312**, 519.
24. E.J.F. Dickinson, H. Ekström and E. Fontes, *Electrochem. Commun.*, 2014, **40**, 71.
25. D.R. Lide, Ed., *CRC Handbook of Chemistry and Physics*, *Internet Version 2005*, CRC Press, Boca Raton, FL, 2005.
26. C.A. Harper, Ed., *Modern Plastics Handbook*, McGraw-Hill, New York, NY, 1999.
27. D.M. Price and M. Jarratt - *Thermochim. Acta*, 2002, **392-393**, 231.

28. S.F. Lau, H. Suzuki and B. Wunderlich, *J. Polym. Sci. Polym. Phys. Ed.*, 1984, **22**, 379.
29. P.M. Kampmeyer, *J. Appl. Phys.*, 1952**, 23**, 99.